Journal of Nuclear Materials 386–388 (2009) 338–341

Contents lists available at ScienceDirect

Journal of Nuclear Materials

journal homepage: www.elsevier.com/locate/jnucmat

Helium effects on microstructural evolution in tempered martensitic steels: In situ helium implanter studies in HFIR

T. Yamamoto [a,*], G.R. Odette [a], P. Miao [a], D.J. Edwards [b], R.J. Kurtz [b]

[a] University of California, Santa Barbara, CA 93106, USA
[b] Pacific Northwest National Laboratory, MS P8-15, P.O. Box 999 Richland, WA 99352, USA

A B S T R A C T

Microstructural evolutions in tempered martensitic steels (TMS) under neutron-irradiation, at fusion relevant He/dpa ratios and dpa rates, were characterized using a novel in situ He-implanter technique. F82H-mod3 was irradiated at 500 °C in HFIR to a nominal 9 dpa and 190 or 380 appm He in both in the as-tempered (AT) and 20% cold-worked (CW) conditions. In all cases, a high number density of 1–2 nm He-bubbles were observed, along with fewer but larger ≈10 nm void-like faceted cavities. The He-bubbles form preferentially on dislocations and various interfaces. A slightly larger number of smaller He bubbles were observed in the CW condition. The lower He/dpa ratio produced slightly smaller and fewer He-bubbles. Comparisons of these observations to the results in nano-structured ferritic alloy (NFA) MA957 provide additional evidence that TMS may be susceptible to He-embrittlement as well as void swelling at fusion relevant He concentrations, while NFA are much more resistant to these degradation phenomena.

1. Introduction

Predicting and mitigating the effects of a combination of large levels of transmutant He and displacement damage (dpa), produced by high energy neutrons, on the dimensional stability and mechanical properties of structural materials is one of the key challenges in the development of fusion energy. The fundamental overriding questions about He–dpa synergisms include: (a) What are the basic interacting mechanisms controlling He and defect transport, fate and consequences, and how are they influenced by the starting microstructure and irradiation variables (dpa rate, He/dpa ratio, temperature and applied stress)? And, (b) how can the detrimental effects of He–dpa synergisms be mitigated and managed by proper microstructural design?

We have previously demonstrated that in situ He implantation in mixed spectrum fission reactor irradiations provides a very attractive approach to assessing the effects of He–dpa synergisms, while avoiding most of the confounding effects associated with Ni- or B-doping type experiments [1–3]. The basic idea is to use a thin Ni, B or Li-containing implanter layer to inject high-energy α-particles into an adjacent sample simultaneously undergoing neutron induced displacement damage. In this case, HFIR irradiations implant He uniformly to a depth of ≈5–8 μm from a μm-scale NiAl coating on TEM discs at controlled He/dpa ratios of 5–50 appm/dpa. The He implanted layer is sufficiently thick for low load Vickers microhardness and nanohardness measurements, as well as for making thinned specimens for extensive microstructural characterization by TEM, and potentially a variety of other techniques. We summarize here the results of microstructural characterization of tempered martensitic steel (TMS), F82H mod3 in both the as-tempered and 20% cold-worked (CW) conditions for HFIR irradiations at 500 °C to 9 dpa and 190–380 appm. These preliminary results focus on TEM characterization of the transport and fate of He in forming cavities (bubbles and voids) and the association of these cavities with dislocations and various interfaces. These observations are also compared to the results in nano-structured ferritic alloy (NFA), MA957, presented elsewhere [1,4,5].

2. Experimental procedures

The TMS examined in this work is a high-Ta variant of F82H (so-called F82H-mod.3) [6]. The base chemical composition of F82H-IEA (nominally, 7.5%Cr 2%W 0.2%V 0.1%C 0.1%Si 0.02%Ta 60 ppm N) was modified with high purification (14 ppm N and 0.001% Ti) and high 0.1% Ta [6]. The steel was austenitized at 1040 °C for 30 min, normalized (air-cooled), and tempered at 740 °C for 1.5 h. A wafer of the as-tempered (AT) F82H was also cold rolled to a 20% of thickness reduction. Three mm diameter, 0.2 mm thick TEM discs were irradiated in the HFIR JP26 experiment at 300, 400 and 500 °C to produce a range of dpa and He/dpa for a large matrix of alloys, including the F82H conditions studied here. For the implantation studies, a thin NiAl intermetallic layer was electron beam co-deposited at the UCSB Materials Processing Laboratory

* Corresponding author.
E-mail address: yamataku@engineering.ucsb.edu (T. Yamamoto).

0022-3115/$ - see front matter © 2009 Published by Elsevier B.V.
doi:10.1016/j.jnucmat.2008.12.134

on discs that were paired with adjacent uncoated discs. Nominal coating thicknesses of 1, 2 and 4 μm produced He/dpa ratios of 10, 20, and 40 at 9 dpa.

TEM specimens were prepared at PNNL using a cross-section thinning technique. This involved bonding the irradiated TEM discs between two half cylinders of Mo rod, and then slicing the composite rod to produce thin, 3-mm discs with a rectangular cross-section of the original irradiated disc in the center. Each composite disc was then dimple ground to thickness of ~100 μm centered on the implanted layer. The implanted region of the specimen foil was then thinned to electron transparency by ion milling with a Gatan Precision Ion Polishing System (PIPS). The PIPS was operated using a 5 keV ion beam in sector milling mode, meaning the ion milling was done only when the ion gun was perpendicular to the cross-section of the sample. This approach was found to offer the best chance of preserving the interface region between the NiAl layer and the TMS substrate. After the sample was thinned into the region of interest, a final ion polish was given using a 1.9 keV ion beam for 20 min to remove any surface deposition of Ar. Microstructural examinations were performed on a JEOL 2010F instrument, operating at 200 keV in transmission, with digitally recorded images. A variety of TEM imaging conditions were used, but the cavities were primarily characterized by the through-focus sequence method. Cavities appear as white regions surrounded by a dark ring in the under-focused condition (−512 to 1024 nm), as dark regions surrounded by white rings in the over-focused condition; the cavities are invisible in the focused condition.

Representative regions in the TEM micrographs, with a total area of ≈ 0.1 μm^2, were selected for detailed analysis of the cavity number densities and size distributions. The local foil thickness was measured by the convergent beam diffraction method. The gray-scale micrographs were converted to black and white images. Cavities appear as white features on a black background. Image-J was used to determine cavity number densities and size distributions.

3. Results and discussion

All the irradiation and alloy conditions contained high concentrations of small cavities in the He-implanted regions. Fig. 1(a) shows a representative micrograph for the AT F82H implanted to 380 appm He (nominal He/dpa = 40 appm/dpa) imaged at a −768 nm under-focus condition. The corresponding features identified as cavities by the through-focus sequence examinations are shown in the white on black image in Fig. 1(b). Analysis of this, and other such images, showed that this irradiation condition produced ≈$5.3 \times 10^{22}/m^3$ small bubbles with an average diameter of ≈2.0 ± 1.4 (one standard deviation) nm. Fig. 1 also shows much fewer but larger 10 nm scale polyhedral-faceted cavities. These features are almost certainly voids.

Note a bubble is defined as a near-equilibrium helium filled cavity, with a gas pressure $P_g \approx 3Z(P_g)mkT/4\pi r_b^3 \approx 2\gamma/r_b$ [7], where γ is the surface energy, r_b is the bubble radius, m is the number of He atoms in the bubble and $Z(P_g)$ is the compressibility factor (>1) for high pressure He [7,8]. In contrast, voids are cavities that are unstably growing due to an excess flux of vacancies over self-interstitial atoms (SIA) flowing to them, arising from a bias of dislocation sinks for the SIA [8]. For a specified sink microstructure and irradiation condition, cavities grow as bubbles up to a critical helium content, m^*, where they convert to growing voids, leading to bimodal cavity size distributions. Thus the incubation dose, dpa_i, prior to the onset of rapid void swelling is governed by the requirement that a significant population of cavities reaches the $m > m^*$

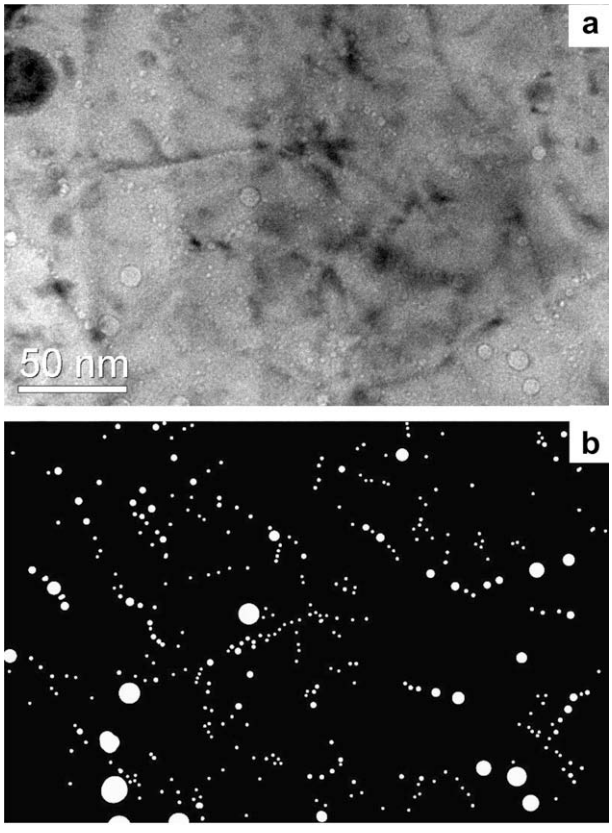

Fig. 1. (a) 512 nm under-focused TEM image for cavity structure in AT F82H-mod.3 irradiated to 9 dpa and He implanted to 380 appm at 500 °C and (b) a map for the features identified as bubbles by through-focus image analysis.

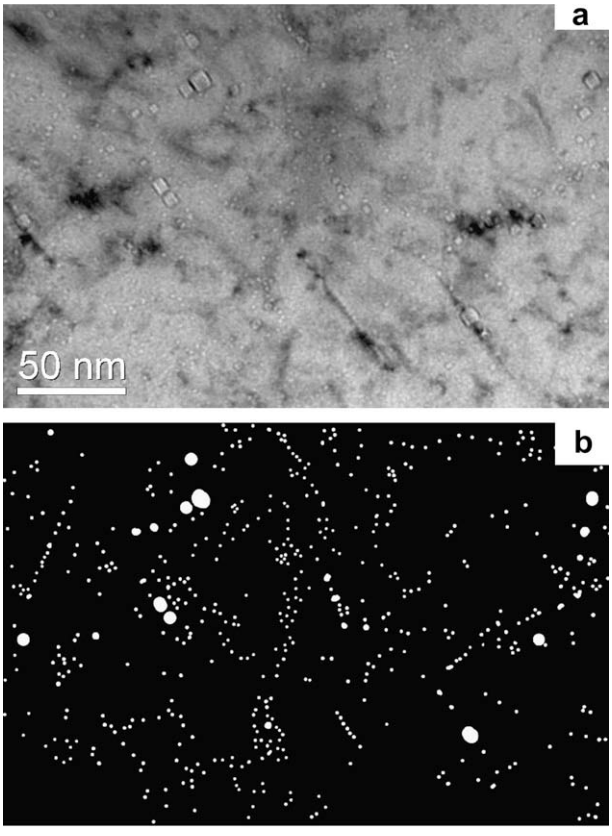

Fig. 2. (a) 512 nm under-focused TEM image for cavity structure in CW F82H-mod.3 irradiated to 9 dpa and He implanted to 380 appm at 500 °C and (b) a map for the features identified as bubbles by through-focus image analysis.

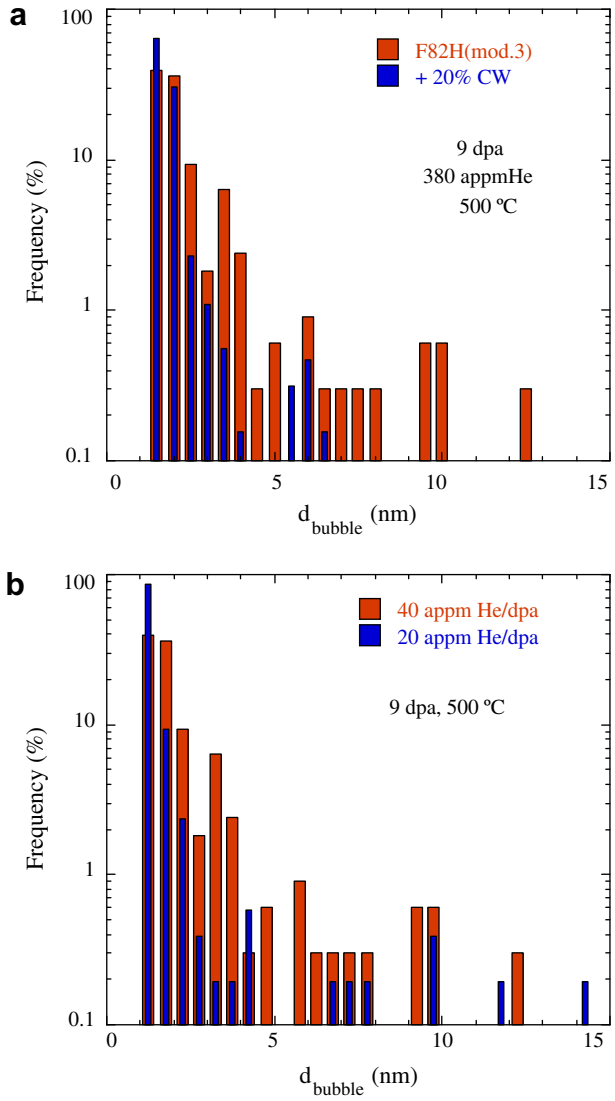

Fig. 3. Cavity size distribution in (a) AT and CW F82H mod.3 irradiated to 9 dpa and He-implanted to 380 appm at 500 °C and (b) at two different He/dpa ratios in AT F82H mod.3 irradiated to 9 dpa at 500 °C.

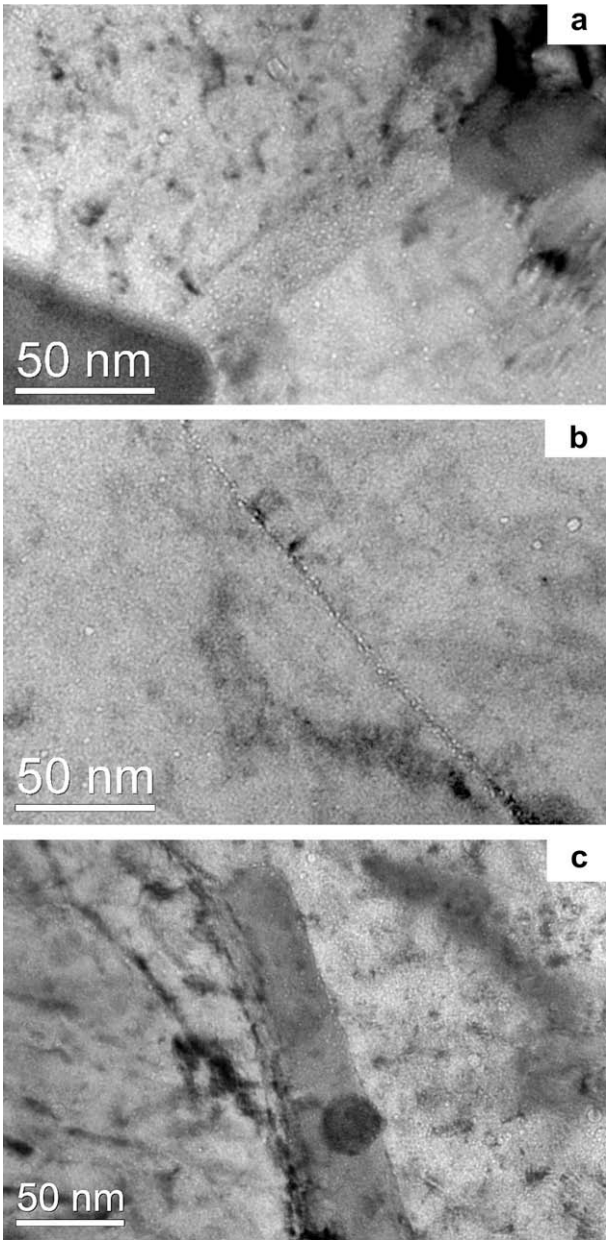

Fig. 4. Cavity formation (a) at grain boundaries in CW F82H mod.3 irradiated to 9 dpa and He-implanted to 380 appm at 500 °C, (b) at grain boundaries AT F82H mod.3 irradiated to 9 dpa and He-implanted to 190 appm at 500 °C, and (c) in the precipitate interface in AT F82H irradiated to 9 dpa and He-implanted to 380 appm at 500 °C.

condition. One corollary is that, for a given number of cavities, the incubation dose, dpa_i, scales inversely with the He/dpa ratio. Another corollary is, that at a specified He/dpa ratio, dpa_i scales with the number of bubbles. Further discussion of the elements of radiation damage resistance can be found in an Annual Review of Materials Research paper [5].

Fig. 1(a) also shows that visible dislocations are highly decorated with *string-of-pearls* like chains of bubbles. The dislocation bubble association is more clearly seen in Fig. 1(b), showing such chains in regions where dislocations are not observed in Fig. 1(a). In these cases, the dislocations may be invisible for the particular imaging condition, or they may have climbed away from previously attached bubbles. In either case, it is clear that a large fraction of the bubble population forms on dislocations. Fig. 1 also suggests that the larger voids are associated with the chains of bubbles. If the dislocations are still attached, this observation suggests some interesting new physics of correlated bubble–void–dislocation evolutions that have not been considered previously.

Fig. 2 shows the corresponding results for the CW F82H are generally similar. However, the bubbles are smaller and more numerous in this case, with a number density of $1.3 \times 10^{23}/m^3$ and average diameter of 1.4 ± 0.7 nm. Likewise, as expected, the AT F82H with a lower He content of 190 appm (nominal 20 appm/dpa) has fewer and smaller cavities, with number densities of 3.9×10^{22} and average diameters of 1.4 ± 1.1 nm. Fig. 3 summarizes the cavity size distributions in these three cases, clearly showing the bimodal bubble–void transition, especially for the lower He/dpa ratio ≈20 appm/dpa.

While the previous discussion has emphasized the dislocation-cavity (bubble and possibly void) associations, small bubbles are also observed on boundaries and matrix–precipitate interfaces. This is illustrated in Fig. 4(a) and (b) showing under-focus cavity images of boundaries in CW F82H at 9 dpa and 380 appm He and AT F82H at 9 dpa and 190 appm, respectively. The slanted boundary between two precipitates in Fig. 4(a) shows a very high density of uniformly distributed fine bubbles. The edge on view of a boundary in

Fig. 4(b) also shows a high concentration of fine bubbles along its entire length. Bubbles at precipitate interfaces are also observed in Fig. 4. Another example of precipitate associated bubbles is shown in Fig. 4(c). The number densities and size distributions of the boundary-interface associated bubbles have not yet been quantified. However, the observation of the collection of large amounts of helium on grain boundaries in TMS alloys, even in the CW condition, is rather alarming for reasons noted in the following section.

The number densities and size distributions for the He/dpa ratio ≈40 appm/dpa for the AT and CW specimens were used to estimate the amount of He in the bubbles, assuming equilibrium capillary pressures, as described previously. The estimated value of 389 ± 84 appm He is in good agreement with the nominal value of 380 appm He.

It should be noted that similar bubble distributions were observed in a previous in situ He injection study of the TMS Eurofer97 [2]. However, the bubbles were somewhat smaller and more numerous in this case. More importantly, preliminary studies of the nano-structured ferritic alloy (NFA) MA957 show an even higher concentration of smaller bubbles compared to Eurofer97, that preferentially form in association with Y–Ti–O enriched nanofeatures (NF) [1,4,5,14]. Most significantly, Odette et al., shows preliminary evidence that the grain boundaries in NFA contain fewer bubbles than in TMS [4,5,14], and appears to be protected from accumulation of high quantities of He by the NF and associated bubbles.

4. Concluding remarks

An in situ He injection technique was used to study the transport and fate of He in the F82H TMS in the AT and CW conditions for irradiation in HFIR to 9 dpa at 500 °C at nominal He/dpa ratios of 20 and 40 appm/dpa. A high density of small bubbles, accompanied by a population of fewer and larger voids, was observed in all cases. A larger concentration of smaller bubbles was found in the CW alloy, and both the size and number densities increased at the higher He/dpa ratio. The bubbles were preferentially associated with dislocations, boundaries and precipitate interfaces. The presence of high concentrations of small bubbles on boundaries is a concern, since this may lead to enormous shifts in the ductile-to-brittle temperature for fast fracture at lower irradiation temperatures, in the hardening regime [9–11], and severe reductions in the creep ductility and rupture time at higher irradiation temperatures [12,13]. Both of these phenomena are related to the weakening of grain boundaries by high concentrations of He, albeit by different mechanisms. These degradation processes may reduce, or even close, the window for application of TMS to fusion first wall structures beyond a dpa limit that may be far less than desired values in the range of 100–200 dpa.

These results barely scratch the surface of what can be learned about the transport, fate and consequences of He using the in situ injection technique. Thus in addition to further characterization studies of the alloys and irradiation conditions described in this and previous publications, a major future effort will be directed at characterizing the large matrix of other alloys and irradiation conditions from the JP26 and JP27 experiments, that contained a total of ≈360 He injected TEM discs.

Acknowledgements

This research was supported by the US Department of Energy, Office of Fusion Energy Sciences, under contracts DE-FG03-94ER54275 and DE-AC06-76RLO1830.

References

[1] T. Yamamoto, G.R. Odette, P. Miao, D.T. Hoelzer, J. Bentley, N. Hashimoto, H. Tanigawa, R.J. Kurtz, J. Nucl. Mater. 367–370 (2007) 399.
[2] R.J. Kurtz, G.R. Odette, T. Yamamoto, D.S. Gelles, P. Miao, B.M. Oliver, J. Nucl. Mater. 367–370 (2007) 417.
[3] T. Yamamoto, G.R. Odette, L.R. Greenwood, Fusion Materials Semiannual Report 1/1 to 6/30/2005 DOE/ER-313/38, 2005, p. 95.
[4] G.R. Odette, P. Miao, T. Yamamoto, D.J. Edwards, R.J. Kurtz, Fusion Materials Semiannual Report 1/1 to 6/30/2008 DOE/ER313/44 (2008) p. 41.
[5] G.R. Odette, M.J. Alinger, B.D. Wirth, Annu. Rev. Mater. Res. 38 (2008) 471.
[6] K. Shiba, M. Enoeda, S. Jitsukawa, J. Nucl. Mater. 329–333 (2004) 243.
[7] R.E. Stoller, G.R. Odette, J. Nucl. Mater. 131 (1985) 118.
[8] G.R. Odette, J. Nucl. Mater. 155–157 (1988) 927.
[9] T. Yamamoto, G.R. Odette, H. Kishimoto, J.-W. Rensman, P. Miao, J. Nucl. Mater. 356 (2006) 27.
[10] Y. Dai, W. Wagner, J. Nucl. Mater., in press.
[11] T. Yamamoto, G.R. Odette, M. Salston, P. Miao, Y. Dai, Trans. Am. Nucl. Soc. 98 (2008) 1111.
[12] H. Trinkaus, J. Nucl. Mater. 118 (1983) 39.
[13] G.R. Odette, J. Nucl. Mater. 122 (1984) 435.
[14] G.R. Odette, P. Miao, T. Yamamoto, D.J. Edwards, H. Tanigawa, R.J. Kurtz, Trans. Am. Nucl. Soc. 98 (2008) 1148.